Interaction of ions and molecules with surface modes in cylindrical channels in solids

Néstor R. Arista
División Colisiones Atómicas, Instituto Balseiro and Centro Atómico Bariloche, Comisión Nacional de Energía Atómica, 8400 San Carlos de Bariloche, Argentina

(Received 22 December 2000; revised manuscript received 6 April 2001; published 14 August 2001)

The interaction of ions and molecules with surface modes in cylindrical channels in solids is described on the basis of the dielectric formalism, starting with simple dielectric models and using also more realistic descriptions of the dielectric properties of various materials of experimental interest. The response of the medium is first characterized in terms of the wake potential, calculating the main effects on the moving particles, including self-energy values, stopping and lateral forces. The general scaling properties of the main quantities as well as the effects of plasmon damping in real materials are described. The formulation is extended to ion clusters and molecular composites, introducing new form factors to take into account the cylindrical symmetry of the problem. Applications to simple ions, diclusters, dipoles, and polar molecules channeled in microcapillaries and nanochannels are considered.

DOI: 10.1103/PhysRevA.64.032901 PACS number(s): 34.50.Bw, 34.50.Dy, 61.85.+p, 79.20.Rf

I. INTRODUCTION

The interaction of charged particles with cylindrical cavities in solids is a subject of interest for current studies of electron and ion interaction with microchannels, capillaries, and nanotubes in various materials. Previous experiments have been made using mostly electrons beams. The excitation of plasmons was observed by transmission of electrons through micropores in thin metal foils (with channel radii of 20–200 nm) [1,2]. More recently, the development of experimental techniques to produce carbon nanotubes with smallest diameters of ~ 1 nm [3–5] has boosted a great number of studies, including electron-energy-loss spectroscopy [6], surface-plasmon excitation [7,8], and preliminary studies of ion channeling [9,10]. In addition, there are also recent studies on the formation of hollow atoms in microcapillaries of various materials [11,12].

Several theoretical studies of the energy loss of charged particles in cylindrical cavities have been published [13–15]. The interaction process has been described mostly in classical terms, and the connection with plasmon excitation was formulated in a semiclassical way. More recently, a comprehensive treatment of the interaction between charged particles and cylindrical surface modes, using both classical and quantum methods, has been carried out [16]. On the other hand, there are extensive studies dealing with the transmission of ion clusters and molecules in thin foils [17] but there are no studies of molecular transmission through narrow channels.

The purpose of this work is to study the interaction of atomic and molecular ions channeled through cylindrical cavities in solids, and to describe the main features of this interaction. The formulation is applied both to simple dielectric-function models as well as to materials of experimental interest where more complicated dielectric functions should be used. The present study will be restricted to nonrelativistic velocities, since this is the range of current interest in connection with ion and molecular-beam studies. A relativistic treatment of the interaction of charged particles with cylindrical cavities has been made in Ref. [18] for the case of electron beams.

This study includes calculations of induced potentials and related quantities (self-energies and energy losses) for several cases of experimental interest, like ion transmission in alumina and silver capillaries. The scaling properties of the induced field and related magnitudes will also be discussed.

The formulation will be extended to the case of molecular ions or composites, introducing new form factors that take into account the cylindrical symmetry of the problem. The formulation will be applied to two cases of possible experimental interest: channeling of diclusters and electric dipoles, or polar molecules, in narrow channels.

The paper is organized as follows: in Sec. II, the properties of the modes of a cylindrical cavity are described, and the analysis is extended to include the effects of damping on the response of the medium. In Sec. III the interaction with external probes is considered, and in Sec. IV we calculate the main self-induced quantities (induced potential, stopping and deflection forces), derive the scaling properties, and calculate the scaling functions. In Sec. V the formulation is extended to the case of molecules or ion clusters, introducing appropriate cylindrical form factors, while Sec. VI refers to the particular cases of diclusters and dipoles. Finally, Sec. VII includes several applications to channeling of ions and molecules in materials of experimental interest.

II. MODES OF A CYLINDRICAL CAVITY

The electrostatic modes of a cylindrical cavity of radius a in a solid are determined by the solutions of the Laplace equation, in terms of cylindrical Bessel functions $I_m(x)$ and $K_m(x)$, with $m=0,\pm 1,\pm 2,\pm 3,\ldots$, as follows [19].

(a) For $\rho<a$.

$$\phi^{(a)}=A_m e^{i(kz+m\varphi)} I_m(k\rho) e^{-i\omega t}; \tag{1}$$

(b) for $\rho>a$.

$$\phi^{(b)}=B_m e^{i(kz+m\varphi)} K_m(k\rho) e^{-i\omega t}; \tag{2}$$

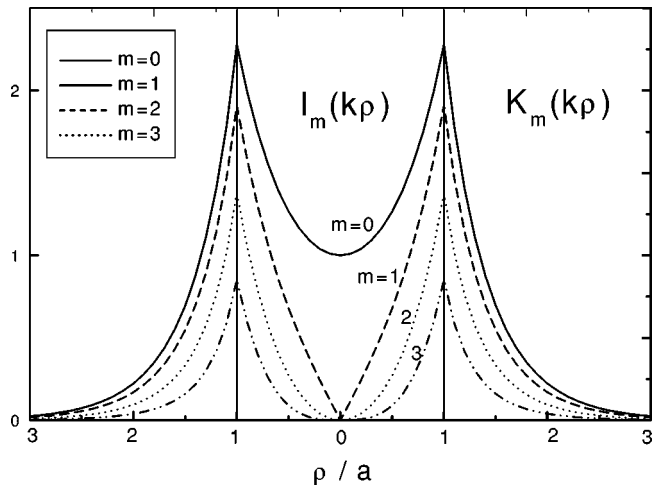

FIG. 1. Electrostatic modes of a cylindrical cavity as a function of the radial coordinate ρ. The internal and external solutions are given by Bessel functions $I_m(k\rho)$ and $K_m(k\rho)$ as illustrated. The mode $m=0$ is the only one that penetrates down to the center of the channel.

where we use cylindrical coordinates (ρ,φ,z) and k is a wave vector along the axial channel direction denoted by z. The relation between the coefficients A_m and B_m, and the frequencies of the modes $\omega_{k,m}=\omega_m(k)$, may be determined by the usual matching conditions for the values of the fields at $\rho=a$. These conditions lead to the following relations [16]:

$$\frac{A_m}{B_m}=\frac{K_m(ka)}{I_m(ka)} \tag{3}$$

and

$$\varepsilon(\omega)=\frac{I_m'(ka)}{I_m(ka)}\frac{K_m(ka)}{K_m'(ka)}, \tag{4}$$

where $\varepsilon(\omega)$ is the dielectric function of the medium; here the primes denote the derivatives with respect to the arguments: $I_m'(x)=dI_m(x)/dx$, $K_m'(x)=dK_m(x)/dx$.

From Eq. (4) one may obtain the *dispersion relation* for each of the modes, $\omega=\omega_m(k)$, which can be solved for each material using the appropriate dielectric function. This may yield real or complex values for $\omega_m(k)$ depending on the dielectric properties of the material.

The main characteristics of these modes are illustrated in Fig. 1, which show the dependence of the electrostatic potential on the radial coordinate ρ. These characteristics are independent of the model dielectric function. The cusp behavior observed at $\rho=a$ is due to the accumulation of electronic charge at the boundary (corresponding to surface-plasmon charge).

A. Plasma-resonance model

The most simple approximation to the dielectric function around a plasma resonance is given by $\varepsilon(\omega)=1-\omega_{P0}^2/\omega(\omega+i\gamma)$ (Drude model), where ω_{P0} is the plasma frequency and γ is the damping constant. In this model, the *energy-loss function* $\mathrm{Im}[-1/\varepsilon(\omega)]$ has a maximum at the shifted plasma-resonance frequency $\omega_P=(\omega_{P0}^2-\gamma^2/4)^{1/2}$.

In a previous work [16] the dispersion relations $\omega_m(k)$ have been shown for the ideal case of negligible damping: $\gamma\ll\omega_P$, $\omega_P\cong\omega_{P0}$; in such case, the frequencies of the modes $\omega_{k,m}\equiv\omega_m(k)$ are real quantities, given by

$$\omega_{k,m}^2=\omega_P^2 x I_m(x)|K_m'(x)|, \tag{5}$$

so that the ratios $\omega_{k,m}/\omega_P$ are given by analytical functions of the general variable $x=ka$. The function $g_m(x)\equiv xI_m(x)|K_m'(x)|$ has the following limits: for $x\to 0$: $g_0(x)\to 1$, $g_m(x)\to 1/2$ $(m\neq 0)$; for $x\to\infty$: $g_m(x)\to 1/2$ (all m). Hence, one gets the following limits: (i) for $ka\to 0$: $\omega_{k,0}\to\omega_P$, $\omega_{k,m}\to\omega_s$ $(m\neq 0)$; (ii) for $ka\to\infty$: $\omega_{k,m}\to\omega_s$ (all m). Here $\omega_s=\omega_P/\sqrt{2}$ is the surface-plasmon frequency of plane surfaces ($a\to\infty$ limit) [20]. Therefore, the frequency of the modes is within the interval $\omega_s<\omega<\omega_P$.

B. Damping effects

Let us consider now the effects of finite damping. In this case the solutions of Eq. (4) yield complex frequencies $\omega_{k,m}=\omega_{k,m}^{(1)}+i\omega_{k,m}^{(2)}$. It may be observed that the imaginary part $\omega_{k,m}^{(2)}$ will be given simply by $-\gamma/2$. In fact, by writing $\omega_{k,m}=\omega_{k,m}^{(1)}-i\gamma/2$, we get $\varepsilon[\Omega]=1-\omega_{P0}^2/\Omega^2$, with $\Omega^2=[(\omega_{k,m}^{(1)})^2+\gamma^2/4]$, and so Eq. (4) yields a solution similar to the case of negligible damping, Eq. (5), but now in terms of the frequency Ω, namely, $\Omega_{k,m}^2=\omega_{P0}^2 g_m(x)$.

Therefore, the solutions for finite damping will be of the form

$$\omega_{k,m}=[\omega_{P0}^2 g_m(x)-\gamma^2/4]^{1/2}-i\gamma/2, \tag{6}$$

with $g_m(x)=xI_m(x)|K_m'(x)|$.

The effects of the damping on the frequency of the modes are shown in Fig. 2 for the modes with $m=0$ and 1. We find in general that the values of the frequencies diminish with increasing damping. It may also be shown that for large damping ($\gamma/\omega_{P0}\gg 1$) the values of $\omega_{k,m}$ become imaginary (overdamped oscillations).

C. Lorentz model

Similar considerations may be applied to the case of the Lorentz model, where the dielectric function is

$$\varepsilon_L(\omega)=1+\frac{\omega_1^2}{\omega_0^2-\omega^2-i\gamma\omega}, \tag{7}$$

with model parameters ω_0 and ω_1. In this case the maximum of the energy-loss function, $\mathrm{Im}[-1/\varepsilon_L(\omega)]$, occurs at a plasma frequency $\omega_P=(\omega_0^2+\omega_1^2-\gamma^2/4)^{1/2}$. Considering again the dispersion relation for the modes of the cavity, $\varepsilon_L(\omega)=I_m'(x)K_m(x)/I_m(x)K_m'(x)$, Eq. (4), and proposing a solution of the form $\omega_{k,m}=\omega_{k,m}^{(1)}-i\gamma/2$, one gets

$$\omega_{k,m}=[\omega_0^2+\omega_1^2 g_m(x)-\gamma^2/4]^{1/2}-i\gamma/2, \tag{8}$$

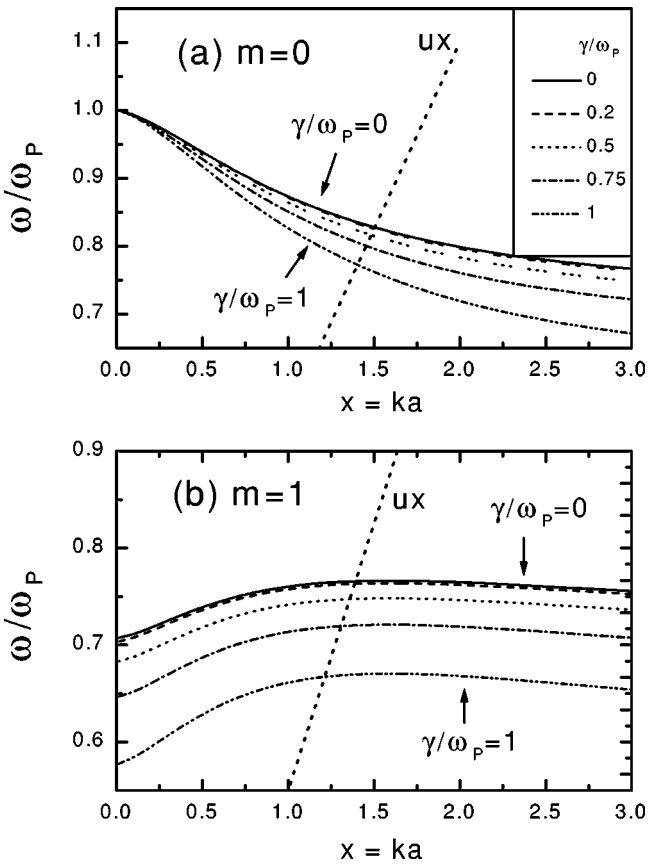

FIG. 2. Damping effects on the dispersion relation for the first two modes, m=0, 1. The figure shows the changes in the frequencies with increasing values of γ/ω_P ($\gamma/\omega_P=0$, 0.2, 0.5, 0.75, and 1). The intersections of ω/ω_P with the line ux yield the values of k and ω that could be excited by a particle with velocity v (resonant excitations) as described in the text.

with $g_m(x)$ defined before. The effects of the damping are essentially similar to those illustrated in Fig. 2 for the Drude model.

These models will be useful to characterize the dominant features of the optical properties of real materials.

III. INTERACTION WITH AN EXTERNAL CHARGE

Let us consider now a particle with charge Ze moving within a cylindrical channel of radius a, with trajectory parallel to the z axis, with velocity v, and with instantaneous coordinates $(\rho_0,\varphi_0,z_0+vt)$.

Since the properties of the medium are represented by a frequency-dependent dielectric function, we introduce the Fourier transforms of the field quantities as follows:

$$F(t)=\int_{-\infty}^{\infty}\frac{d\omega}{2\pi}e^{-i\omega t}F(\omega). \tag{9}$$

A. Induced potential

As described previously [16], the induced potential inside ($\rho<a$) and outside ($\rho>a$) the cavity may be expanded in terms of cylindrical Bessel functions $I_m(x)$ and $K_m(x)$. These fields must satisfy the usual boundary conditions, and in this way one obtains the following results for the internal ($\phi_{ind}^{(a)}$) and external ($\phi_{ind}^{(b)}$) solutions.

(a) $\rho<a$. The total potential for $\rho<a$ becomes $\phi_{tot}^{(a)}(\rho,\varphi,z,t)=\phi_{ext}(\rho,\varphi,z,t)+\phi_{ind}^{(a)}(\rho,\varphi,z,t)$, where ϕ_{ext} is the bare Coulomb potential of the external charge and $\phi_{ind}^{(a)}$ is the induced potential given in the frequency domain by [16]

$$\phi_{ind}^{(a)}(\rho,\varphi,z,\omega)=2Ze\sum_{m=-\infty}^{\infty}\int_0^{\infty}dkI_m(k\rho_0)I_m(k\rho)e^{im(\varphi-\varphi_0)}\times\tilde{A}_m(k,\omega)\{\exp[ik(z-z_0)]\delta(\omega-kv)+\exp[-ik(z-z_0)]\delta(\omega+kv)\} \tag{10}$$

and integrating in ω, according to Eq. (9),

$$\phi_{ind}^{(a)}(\rho,\varphi,z,t)=\frac{2}{\pi}Ze\sum_{m=-\infty}^{\infty}\int_0^{\infty}dkI_m(k\rho_0)I_m(k\rho)e^{im(\varphi-\varphi_0)}\times\{\mathrm{Re}[\tilde{A}_m(k,\omega)]\cos(kz-\omega t)-\mathrm{Im}[\tilde{A}_m(k,\omega)]\sin(kz-\omega t)\}\big|_{\omega=kv}, \tag{11}$$

where we have used the properties $\tilde{A}_m(k,\omega)+\tilde{A}_m(k,-\omega)=2\mathrm{Re}[\tilde{A}_m(k,\omega)]$, $\tilde{A}_m(k,\omega)-\tilde{A}_m(k,-\omega)=2i\mathrm{Im}[\tilde{A}_m(k,\omega)]$, and the value of the frequency is now linked to k by $\omega=kv$.

(b) $\rho>a$. In this case one obtains for the total potential the analogous expression

$$\phi_{tot}^{(b)}(\rho,\varphi,z,t)=\frac{2}{\pi}Ze\sum_{m=-\infty}^{\infty}\int_0^{\infty}dkI_m(k\rho_0)K_m(k\rho)e^{im(\varphi-\varphi_0)}\times\{\mathrm{Re}[\tilde{B}_m(k,\omega)]\cos(kz-\omega t)-\mathrm{Im}[\tilde{B}_m(k,\omega)]\sin(kz-\omega t)\}\big|_{\omega=kv}. \tag{12}$$

The amplitude coefficients $\tilde{A}_m(k,\omega)$ and $\tilde{B}_m(k,\omega)$ in Eqs. (11) and (12) are determined from the boundary conditions, which yield

$$\tilde{A}_m(k,\omega)=\frac{[1-\varepsilon(\omega)]K_m(ka)K_m'(ka)}{\varepsilon(\omega)I_m(ka)K_m'(ka)-K_m(ka)I_m'(ka)}, \tag{13}$$

$$\tilde{B}_m(k,\omega)=\frac{I_m(ka)K_m'(ka)-K_m(ka)I_m'(ka)}{\varepsilon(\omega)I_m(ka)K_m'(ka)-K_m(ka)I_m'(ka)}. \tag{14}$$

B. Coherent excitations, resonances, and wakes

According to Eqs. (10) and (11), the values of the induced field consist of a superposition of wave components that satisfy the condition $\omega=kv$. This means that only waves with phase velocities ω/k coincident with the particle velocity v will be excited by the particle. It may be shown that the form

of the induced potential Eq. (11) has a typical ''wake'' structure, characterized by a function of ρ and $z-z_0-vt$ that remains stationary in a frame of reference moving together with the particle at velocity v. These characteristics apply irrespective of the dielectric function used to represent the properties of the medium, but the shape of the wake potential depends strongly on this [21]. (The properties of the wake potential have been studied previously only for particles moving in homogeneous media [22].)

By comparing Eqs. (4) and (13) we see that the equation for the modes coincides with the poles of the ''response functions'' $\tilde{A}_m(k,\omega)$. This corresponds to the *resonant excitation* of those modes. In particular, if one uses the plasma-resonance model considered before, the values of k and ω that satisfy the resonance condition may be determined for each velocity v by solving the equation $\omega_m(k)=kv$. This condition is illustrated in Fig. 2 by the line $\omega/\omega_P=kv/\omega_P=ux$, with $u=v/\omega_P a$ and $x=ka$. Then, the values of k and ω are given in this case by the intersection of the line $\omega/\omega_P=ux$ with the corresponding dispersion-relation curve for each mode m. In this way k and ω become velocity-dependent functions: $k=k_m[v]$, $\omega=\omega_m[v]$.

The general properties of the wake potential are illustrated in Fig. 3, for a proton with velocity $v=5$ a.u. in a channel of radius $a=10$ a.u. Calculations were done for a medium with $\omega_P=0.5$ a.u., $\gamma=0.05$. The instantaneous position of the particle is $z=0$, $\rho=0$ (solid circle). The figure shows the values of the induced potential behind the particle. As it may be observed, the potential has a ''normal'' wake behavior outside the cavity ($\rho>a$) but it becomes very flat inside it. The cusp behavior at $\rho=a$ is due to the accumulation of surface charge at the boundary (cf. also Fig. 1). Panels (b) and (c) of this figure show the lateral and front views of the wake potential. It may be observed that the wavelength of the wake in the z direction is given by $2\pi v/\omega_P$, as in the case of homogeneous media.

A detailed comparison between the wakes induced in a homogeneous medium and in a cylindrical cavity is shown in Fig. 4, which shows a cut of the wake potential in the transverse plane for two values of z ($z=0$ and $z=-50$ a.u.). This confirms that the values of the induced potential outside the cavity are very similar to those in homogeneous media, whereas inside the cavity the screening appears ''frozen,'' which is due to the fact that the electrons cannot penetrate into the cavity (outer screening).

IV. SELF-INDUCTION EFFECTS

From the general expression for the induced potential we may obtain some relevant quantities that represent the main effects of the field on the moving charge. The quantities of interest are the self-induced potential (which is the source of a self-energy interaction), and the longitudinal and transverse components of the electric field acting on the charge (which produce the corresponding stopping and deflection forces). We denote these quantities using an upper index 0, namely: $\phi_{ind}^{(0)}\equiv\phi_{ind}(\mathbf{r},t)|_{\mathbf{r}=\mathbf{v}t}$, $E_z^{(0)}\equiv ZeE_z(\mathbf{r},t)|_{\mathbf{r}=\mathbf{v}t}$, and $E_\rho^{(0)}\equiv ZeE_\rho(\mathbf{r},t)|_{\mathbf{r}=\mathbf{v}t}$. The expressions for these quantities are the following.

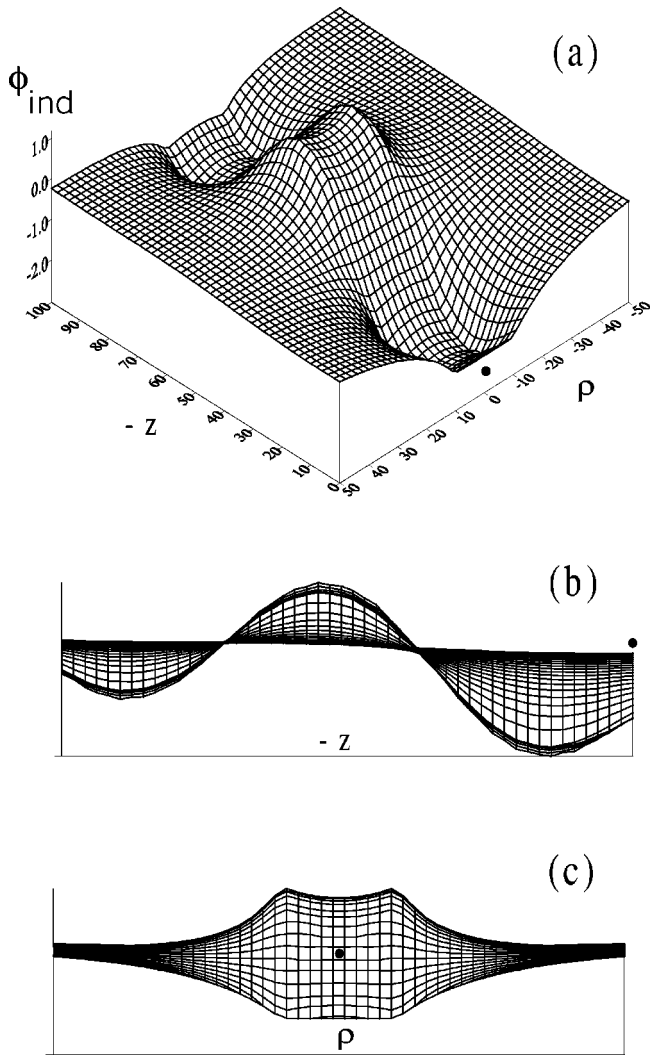

FIG. 3. Calculation of the wake potential for a proton with velocity $v=5$ a.u. in a channel of radius $a=10$ a.u., for a medium with $\omega_P=0.5$ a.u., $\gamma=0.05$. The instantaneous position of the particle is $z=0$, $\rho=0$, and is illustrated by a solid circle in each figure. Panel (a) shows a general pattern of the induced potential; panels (b) and (c) show lateral and front views of the wake. The wavelength of the wake in the z direction is given by $2\pi v/\omega_P$, and the lateral decay distance is v/ω_P.

(a) Induced potential on the charge.

$$\phi_{ind}^{(0)}=\frac{2}{\pi}Ze\sum_{m=-\infty}^{\infty}\int_0^\infty dk[I_m(k\rho_0)]^2\,\mathrm{Re}[\tilde{A}_m(k,kv)], \tag{15}$$

and the *self-energy* is given by

$$W_{self}=\frac{1}{2}Ze\,\phi_{ind}^{(0)}.$$

(b) Longitudinal electric field ($E_z^{(0)}$) and *stopping force* (F_z) on the particle.

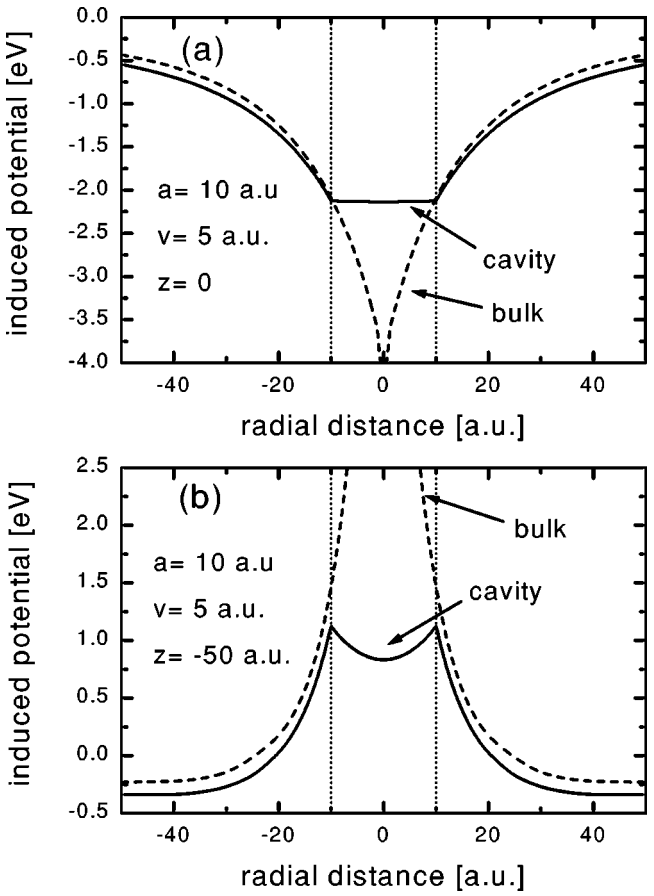

FIG. 4. Comparison between the wakes induced in a homogeneous media (dashed line) and in a cylindrical cavity (solid line). The figures show two cuts of the induced potential along transverse planes located at $z=0$ (containing the position of the charge) and $z=-50$ a.u. (behind it). The sharp behavior at $\rho=a=10$ a.u. is produced by the accumulation of surface-plasmon charge at the wall.

$$F_z \equiv ZeE_z^{(0)} = \frac{2}{\pi}(Ze)^2 \sum_{m=-\infty}^{\infty} \int_0^{\infty} dk k [I_m(k\rho_0)]^2 \, \mathrm{Im}[\tilde{A}_m(k,kv)]. \tag{16}$$

(c) Transverse electric field ($E_\rho^{(0)}$) and *deflection force* (F_ρ) on the particle.

$$F_\rho \equiv ZeE_\rho^{(0)} = -\frac{2}{\pi}(Ze)^2 \sum_{m=-\infty}^{\infty} \int_0^{\infty} dk k I_m(k\rho_0) I_m'(k\rho_0) \times \mathrm{Re}[\tilde{A}_m(k,kv)]. \tag{17}$$

It may be noted that the lateral force vanishes when the particle moves along the axis of the channel ($\rho_0=0$) due to the behavior of $I_m'(x)$ for $x\to 0$. We may also note an interesting relation between $E_\rho^{(0)}$ and $\phi_{ind}^{(0)}$,

$$E_\rho^{(0)} = -\frac{1}{2}\frac{\partial \phi_{ind}^{(0)}}{\partial \rho_0}. \tag{18}$$

The physical meaning of this equation can be made clear by expressing it in terms of the self-energy and transverse force as: $F_\rho = -\partial W_{self}/\partial \rho_0$, which relates the transverse force to the variation of the interaction energy in a small lateral displacement. This relation expresses the conservative character of the transverse force, associated with variations in the self-energy of the particle due to its interaction with the cavity wall.

A further analysis indicates that we may consider a decomposition of the forces into a *dissipative* component, related to the motion in the z direction, and a *conservative* force component in the perpendicular plane (for the case of parallel motion). These components are represented by the imaginary and real parts of $\tilde{A}_m(k,\omega)$ respectively in Eqs. (16) and (17).

By comparing the results for the stopping force, Eq. (16), with those corresponding to charged particles in homogeneous media we observe that $\mathrm{Im}[\tilde{A}_m(k,\omega)]$ plays here the role of the energy-loss function, $\mathrm{Im}[-1/\varepsilon(q,\omega)]$, in previous calculations. Therefore, the denomination of ''response functions'' used for $\tilde{A}_m(k,\omega)$ is justified.

A. Reduced variables and scaling properties

We may write the previous results in a more general way by introducing the following variables: $u \equiv v/\omega_c a$, $x \equiv ka$, $\xi \equiv \rho_0/a$; where ω_c denotes a characteristic frequency of the material (in the plasma-resonance model ω_c is given by the plasma frequency). The variable $u=v/v_s$ will be referred to as the *reduced velocity*, introducing also the *scaling velocity* $v_s=\omega_c a$.

In terms of these variables, the equations for the induced potential, and for the longitudinal and transverse fields, Eqs. (15)–(17) may be cast in the following form.

$$\phi_{ind}^{(0)} = \frac{Ze}{a} f_{pot}(u,\xi), \tag{19}$$

$$E_z^{(0)} = \frac{Ze}{a^2} f_z(u,\xi), \tag{20}$$

$$E_\rho^{(0)} = \frac{Ze}{a^2} f_\rho(u,\xi), \tag{21}$$

where the scaling functions are given by

$$f_{pot}(u,\xi) = \frac{2}{\pi} \sum_{m=-\infty}^{\infty} \int_0^{\infty} dx [I_m(x\xi)]^2 \, \mathrm{Re}[\tilde{A}_m(x,xu)], \tag{22}$$

$$f_z(u,\xi) = \frac{2}{\pi} \sum_{m=-\infty}^{\infty} \int_0^{\infty} dx x [I_m(x\xi)]^2 \, \mathrm{Im}[\tilde{A}_m(x,xu)], \tag{23}$$

$$f_\rho(u,\xi) = -\frac{2}{\pi}\sum_{m=-\infty}^{\infty}\int_0^\infty dx x I_m(x\xi) I'_m(x\xi)\mathrm{Re}[\tilde{A}_m(x,xu)]. \tag{24}$$

Due to Eq. (18) there is also the following relation between these functions,

$$f_\rho(u,\xi) = -\frac{1}{2}\frac{\partial f_{pot}(u,\xi)}{\partial \xi}. \tag{25}$$

These expressions take into account the scaling properties already noted, so that the induced potential, electric field, and forces may all be expressed in terms of a set of scaling functions $f_i(u,\xi)$. These functions may be calculated for each material using appropriate dielectric functions. Size dependence of the solutions (on the cavity radius a) is simply represented by the factors $1/a$ and $1/a^2$ in Eqs. (19)–(21).

B. Simple models

The scaling properties described so far apply to any type of dielectric function $\varepsilon(\omega)$. But if the previous models are used, the values of $\tilde{A}_m(k,\omega)$ may be cast in a very simple form. The expressions for the Drude and Lorentz models are the following.

a. Drude model. In this case one gets

$$\tilde{A}_m(k,\omega) = \tilde{A}_m[x,ux] = \frac{g_m(x)}{ux(ux+i\delta)-g_m(x)}\frac{K_m(x)}{I_m(x)}, \tag{26}$$

where $x=ka$, $ux=kv/\omega_{P0}=\omega/\omega_{P0}$, $\delta=\gamma/\omega_{P0}$, and $g_m(x)\equiv xI_m(x)|K'_m(x)|$.

b. Lorentz model. In this case

$$\tilde{A}_m(k,\omega) = \tilde{A}_m[x,ux] = \frac{g_m(x)}{ux(ux+i\delta)-[g_m(x)+\omega_0^2/\omega_1^2]}\frac{K_m(x)}{I_m(x)}, \tag{27}$$

where $ux=kv/\omega_1=\omega/\omega_1$, $\delta=\gamma/\omega_1$ and $g_m(x)\equiv xI_m(x)|K'_m(x)|$.

These expressions show explicitly the parametrization of $\tilde{A}_m(k,\omega)$ in terms of the general variables $x=ka$ and $u=v/v_s$ (reduced velocity) for the simple models described before. It may be shown that the poles of the response functions $\tilde{A}_m(k,\omega)$, Eqs. (26) and (27), correspond to complex frequencies given, respectively, by Eqs. (6) and (8).

C. Scaling functions

Figure 5 shows the functions $f_{pot}(u,\xi)$, $f_z(u,\xi)$, and $f_\rho(u,\xi)$, corresponding to the plasma-resonance model, $\varepsilon(\omega)=1-\omega_P^2/\omega(\omega+i\gamma)$ with $\delta=\gamma/\omega_P\to 0$.

The functions $f_{pot}(u,\xi)$, $f_z(u,\xi)$, and $f_\rho(u,\xi)$ show in a general way the characteristics of the induced potential (and self-energy), and the longitudinal and transverse forces acting on a moving particle with reduced velocity u and reduced radial coordinate $\xi=\rho_0/a$. The values of $\phi_{ind}^{(0)}$ and $E_z^{(0)}$ and $E_\rho^{(0)}$ may be evaluated from these results and using the relations (19), (20), and (21).

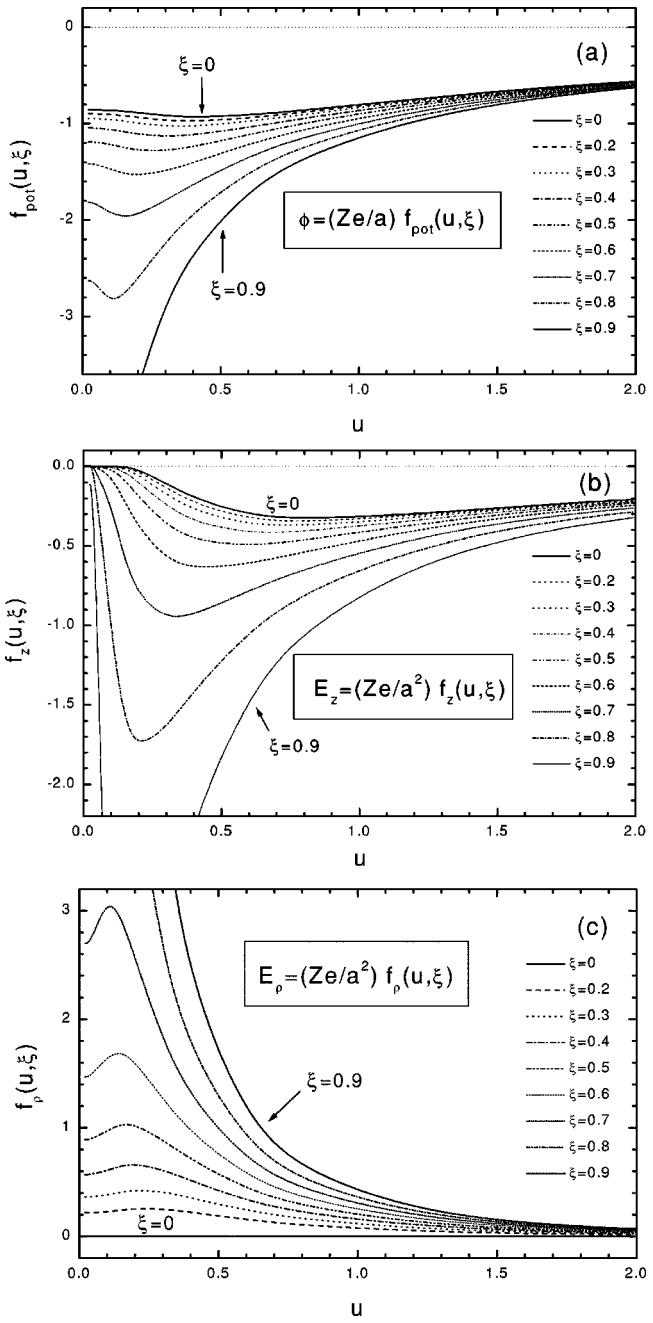

FIG. 5. Scaling functions $f_{pot}(u,\xi)$, $f_z(u,\xi)$, and $f_\rho(u,\xi)$, for the calculation of the induced potential, longitudinal force, and transverse force acting on a moving particle with reduced velocity u and reduced radial coordinate $\xi=\rho_0/a$, according to the plasma-resonance model, $\varepsilon(\omega)=1-\omega_P^2/\omega(\omega+i\gamma)$ with $\delta=\gamma/\omega_P\to 0$. The insets give the relations that may be used to calculate the values of $\phi_{ind}^{(0)}$, $E_z^{(0)}$ and $E_\rho^{(0)}$ using these scaling functions, Eqs. (19)–(21).

As a general behavior, we observe in all cases an important increase of the values shown in Fig. 5 as the particle approaches the boundary of the channel ($\xi\to 1$). This is in

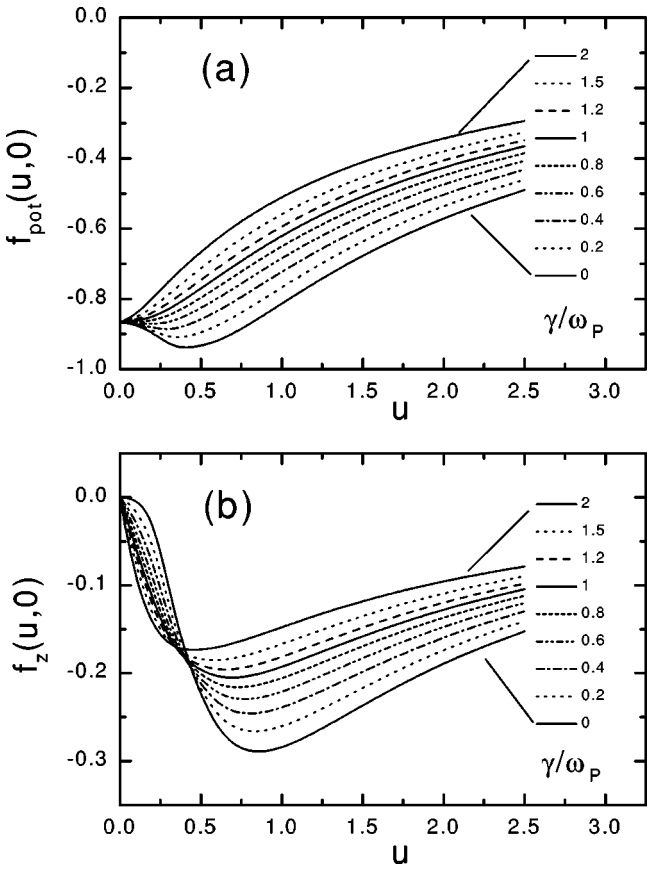

FIG. 6. Effects of damping on the values of the potential and stopping functions f_{pot}, f_z, for particles moving along the channel axis ($\xi=0$), for a set of values of γ/ω_P. The curves for $\gamma/\omega_P=0$ correspond to the case of undamped plasma oscillations. With increasing damping values the dip in the potential at $u\sim 0.5$, and the threshold behavior in the stopping force (for $u\ll 1$), are washed out. For large values of γ/ω_P the function f_z at low velocities shows the "friction force" characteristics $f_z \propto u$.

agreement with the diverging behavior already noted in this limit in Ref. [16]. The "stopping function" $f_z(u,\xi)$ shows the general characteristics of a stopping force, with a maximum at intermediate velocities (in particular, for $\xi=0$, i.e., for particles moving along the channel axis, one gets $u_{\max}\cong 0.8$), and a Bethe-type decreasing behavior at high energies. Note however that the position of the maximum shifts to smaller velocities with increasing values of ξ. Due to the relation between u and v, this shows that the maximum value of the stopping force for the $\xi=0$ case will occur for particle velocities close to the scaling velocity $v_s=\omega_P a$. Note also that since $v_{\max}$ is proportional to the channel radius, one may expect relativistic values of $v_{\max}$ for channel radii $a>100$ a.u.

D. Analytical results for the stopping force

The integration of the stopping force $F_z=ZeE_z$ may be carried out in analytical terms in the particular case of a sharp plasma resonance [16] and one obtains

$$F_z=\sum_{m=-\infty}^{\infty} F_{z,m} = -\left(\frac{Ze\omega_P}{v}\right)^2 \sum_{m=-\infty}^{\infty} xK_m(x)|K_m'(x)|[I_m(x\xi)]^2|_{x=x_m}, \tag{28}$$

so that the function $f_z(u,\xi)$ is in this case given by

$$f_z(u,\xi)=-\frac{1}{u^2}\sum_{m=-\infty}^{\infty} xK_m(x)|K_m'(x)|[I_m(x\xi)]^2|_{x=x_m(u)}. \tag{29}$$

The dependence on u in this expression is given parametrically through the functions $x_m(u)$. This arises from the intersection condition: $\omega_{k,m}(x)=kv=ux\omega_P$ (Fig. 2) that yields the values of x_m for each mode as a function of the reduced velocity u.

Useful analytical results may also be obtained for two cases of particular interest.

a. Motion along the axis ($\rho_0=0$). In this case only the $m=0$ term contributes, yielding a stopping force

$$F_z\cong -\left(\frac{Ze\omega_P}{v}\right)^2 K_0\left(\frac{a\omega_P}{v}\right). \tag{30}$$

It is interesting to note here the exponential *threshold* behavior for $v\ll v_s=\omega_P a$ (due to the behavior of $K_0(x)\sim \exp(-x)/\sqrt{x}$ for $x\gg 1$); this is a characteristic of the undamped harmonic-oscillator model. On the other hand, for $v\gg v_s$ one obtains the Bohr limit, with $K_0(\omega_P a/v)\sim \ln(1.123v/\omega_P a)$.

b. Motion near the border ($\rho_0\sim a$). In the proximity of the cavity wall a large number of terms *m* contribute to the force, yielding a divergent behavior of the form

$$F_z\cong -\left(\frac{Ze\omega_s}{v}\right)^2 K_0\left(\frac{2\omega_s}{v}|\rho_0-a|\right). \tag{31}$$

This limit corresponds to the stopping force for a particle moving parallel to an infinite *plane* surface [23], at a distance $|\rho_0-a|$.

E. Damping effects

The previous analytical results apply to the special case of sharp plasma resonances ($\delta=\gamma/\omega_P\to 0$). But in most cases of experimental interest there is a significant broadening of this resonance. To quantify the expected differences in these cases, the previous calculations have been extended to cases with $\gamma\neq 0$, using the values of γ/ω_P as a parameter.

These differences are illustrated in Fig. 6, which shows the results for the potential function f_{pot}, and for the stopping function f_z, for particles moving along the channel axis ($\xi=0$), considering a set of values of γ/ω_P. As a general result we find a decreasing behavior of the magnitudes with increasing γ values (although not a monotonous one in the case of the stopping function). We observe that the dip in the

potential at $u \sim 0.5$ is progressively eliminated, whereas in the case of the stopping function we note two effects: a shift to lower velocities of the absolute minimum of f_z (corresponding to the stopping-power maximum), and, more significantly, the disappearance of the threshold behavior at low velocities observed for small damping values, turning into a ''frictionlike'' force proportional to velocity when the damping effect is large ($\gamma/\omega_P > 1$). It is interesting to note that a similar behavior (proportionality with velocity) was obtained in the case of particles moving with trajectories parallel to a plane surface when the damping was important [24].

V. INTERACTION WITH CLUSTERS AND MOLECULES

We will consider next the excitation of capillary modes produced by atomic and molecular composites (neutral or ionized), including the cases of discrete or continuous charge distributions.

A. Discrete distributions

The generalization of Eq. (10) for a cluster of N ions with charges $Z_i e$ and trajectories given by: $\rho = \rho_i, \varphi = \varphi_i, z = z_i + vt$ (i.e., with a common velocity v) is straightforward. First we determine the potential induced by the whole cluster within the cavity as follows:

$$\begin{aligned}\phi_{ind}^{(cluster)}(\rho,\varphi,z,t) = 2\sum_{i=1}^{N} Z_i e \int_{-\infty}^{\infty} \frac{d\omega}{2\pi} e^{-i\omega t} \sum_{m=-\infty}^{\infty} e^{im(\varphi-\varphi_i)} \\ \times \int_0^{\infty} dk I_m(k\rho) I_m(k\rho_i) \times \tilde{A}_m(k,\omega) \\ \times \{\exp[ik(z-z_i)]\delta(\omega - kv) \\ + \exp[-ik(z-z_i)]\delta(\omega + kv)\} \end{aligned} \tag{32}$$

from which one can derive the electric field and other related quantities. In particular we will pay attention here to the total stopping and lateral forces and to the self-energy of the interacting system.

1. Stopping force

The total stopping force on the cluster may be calculated by $\mathbf{F}_{cluster} = \Sigma_{j=1}^{N} \mathbf{F}_j$, where $\mathbf{F}_j = -Z_j e \nabla \phi_{ind}|_{\vec{r}=\vec{r}_j}$. The z component of the total force gives the average energy loss or cluster-stopping power

$$\left.\frac{dE}{dz}\right|_{cluster} = \sum_{j=1}^{N} \mathbf{F}_j \cdot \hat{\mathbf{z}} = -\sum_{j=1}^{N} Z_j e \left.\frac{\partial \phi_{ind}}{\partial z}\right|_{\vec{r}=\vec{r}_j}. \tag{33}$$

Inserting Eq. (32) for ϕ_{ind} and performing the ω integration one finally obtains

$$\begin{aligned}\left.\frac{dE}{dz}\right|_{cluster} = \frac{2e^2}{\pi} \sum_{m=-\infty}^{\infty} \int_0^{\infty} dk k \\ \times |\mathcal{F}_m^{(cl)}(k)|^2 \mathrm{Im}[\tilde{A}_m(k,\omega)]|_{\omega=kv}, \end{aligned} \tag{34}$$

where $\mathcal{F}_m^{(cl)}(k)$ are the *cluster form factors*, which we define here as

$$\mathcal{F}_m^{(cl)}(k) = \sum_{i=1}^{N} Z_i I_m(k\rho_i) e^{-ikz_i} e^{-im\varphi_i}. \tag{35}$$

It may be observed that for a single ion i the form factor reduces to, $|\mathcal{F}_m^{(i)}(k)|^2 = Z_i^2 [I_m(k\rho_i)]^2$, so that one retrieves the previous result of Eq. (16).

2. Lateral force

Proceeding in a similar way one obtains the lateral force on the cluster,

$$\begin{aligned} F_{lat} &= \sum_{j=1}^{N} \mathbf{F}_j \cdot \hat{\boldsymbol{\rho}} \\ &= -\frac{e^2}{\pi} \sum_{m=-\infty}^{\infty} \int_0^{\infty} dk \mathcal{F}_m^{(cl)*} \nabla_\rho \mathcal{F}_m^{(cl)} \mathrm{Re}[\tilde{A}_m(k,\omega)]|_{\omega=kv}, \end{aligned} \tag{36}$$

where

$$\nabla_\rho \mathcal{F}_m^{(cl)} = k \sum_{i=1}^{N} Z_i I_m'(k\rho_i) e^{-ikz_i} e^{-im\varphi_i} \tag{37}$$

3. Self-energy

Finally, the self-energy for the distribution of discrete charges is calculated as

$$W_{cluster} = \frac{1}{2} \sum_{i,j} Z_j e \phi_{ind}^{(i)}(\rho_j, \varphi_j, z_j, t), \tag{38}$$

where $\phi_{ind}^{(i)}(\rho_j, \varphi_j, z_j, t)$ denotes the induced potential produced by particle i acting on particle j.

This yields the following result:

$$W_{cluster} = \frac{e^2}{\pi} \sum_{m=-\infty}^{\infty} \int_0^{\infty} dk |\mathcal{F}_m^{(cl)}(k)|^2 \mathrm{Re}[\tilde{A}_m(k,\omega)]|_{\omega=kv} \tag{39}$$

in terms of the cluster form factors previously defined.

As a generalization of Eq. (18), F_{lat} and $W_{cluster}$ satisfy the conservative relation

$$F_{lat} = -\nabla_\rho W_{cluster} \tag{40}$$

(note that ∇_ρ denotes here a derivative with respect to the radial displacement of the whole cluster).

B. Continuous distributions

The previous considerations may be extended also to the case of continuous distributions of charge moving with velocity v. Thus, for instance, the self-energy for an external charge distribution of the form $e\rho_{ext}(\mathbf{r} - \mathbf{v}t)$, with $\mathbf{v}$ parallel to the z axis, is given by

$$W=\frac{1}{2}\int d^3\mathbf{r}e\rho_{ext}(\mathbf{r},t)\phi_{ind}(\mathbf{r},t), \tag{41}$$

where

$$\phi_{ind}(\mathbf{r},t)=2\int d^3\mathbf{r}'e\rho_{ext}(\mathbf{r}',t)\int_{-\infty}^{\infty}\frac{d\omega}{2\pi}e^{-i\omega t}\times\int_0^{\infty}dk\sum_{m=-\infty}^{\infty}e^{im(\varphi-\varphi')}\times\tilde{A}_m(k,\omega)I_m(k\rho)I_m(k\rho')[e^{ik(z-z')}\delta(\omega-kv)+e^{-ik(z-z')}\delta(\omega+kv)]. \tag{42}$$

This yields after some algebra the same result as in Eq. (39), where now

$$\mathcal{F}_m(k)=\int d^3\mathbf{r}\rho_{ext}(\mathbf{r})I_m(k\rho)e^{-ikz}e^{-im\varphi}. \tag{43}$$

These are the form factors for extended charge distributions. In particular, if one takes $\rho_{ext}(\mathbf{r})$ given by $\Sigma_i Z_i\delta(\mathbf{r}-\mathbf{r}_i)$, one retrieves the form factors of Eq. (35).

C. Form factors

It is illustrative to compare the present results with those corresponding to ion clusters in infinite homogeneous solids [17]. Thus, for instance, by comparing the results for the stopping force we observe that $\mathrm{Im}[\tilde{A}_m(k,\omega)]$ plays here the role of an energy-loss function (replacing $\mathrm{Im}[-1/\varepsilon(q,\omega)]$); in addition, the form factors $\mathcal{F}_m^{(cl)}(k)$ obtained here differ appreciably from the corresponding quantities for homogeneous systems, where the form factors have the well-known Fourier-transform expression (plane-wave form factors), namely,

$$\mathcal{F}(\mathbf{q})=\int d^3\mathbf{r}\rho_{ext}(\mathbf{r})e^{-i\mathbf{q}\cdot\mathbf{r}}. \tag{44}$$

The special forms of the *cylindrical form factors* obtained here, Eqs. (35) and (43), express the lack of translational invariance in the plane perpendicular to the channel axis. Note in Eqs. (35) and (43) that only the z dependence maintains the characteristic aspect of a translation factor e^{-ikz}, whereas the azimuthal dependence takes into account the 2π periodicity of the present problem.

An additional difference to be considered is that the cylindrical form factors derived here depend on the transverse coordinates ρ_i of the charges (no translational invariance), so that they must be calculated for each position of the cluster in the transverse plane.

VI. APPLICATIONS: DIATOMIC SYSTEMS

Let us consider now the application of the previous developments to two cases of special interest: (i) a ''dicluster'' consisting of two ions with charges Z_1 and Z_2 moving in a correlated way through the channel, and (ii) the case of ''dipole channeling.''

A. Diclusters

From the previous formulation we write the form factor for this case as

$$\mathcal{F}_m^{(2-cl)}(k)=Z_1I_m(k\rho_1)e^{-ikz_1}e^{-im\varphi_1}+Z_2I_m(k\rho_2)e^{-ikz_2}e^{-im\varphi_2}. \tag{45}$$

We will analyze here the case of swift diclusters moving along the channel axis, with an internuclear distance r_0, considering in particular the following cases.

(a) Aligned dicluster; i.e., a D cluster with internuclear axis oriented in the z direction ($\rho_1=\rho_2=0$, $z_1-z_2=r_0$). In this case one finds that only the $m=0$ term contributes, with a form-factor value

$$\mathcal{F}_0^{(2-cl)}(k)=[Z_1e^{-ikz_1}+Z_2e^{-ikz_2}]. \tag{46}$$

More particularly, for $Z_1=\pm Z_2$ we get $\mathcal{F}_0^{(2-cl)}(k)=2Z_1\cos(kr_0/2)$, and $\mathcal{F}_0^{(2-cl)}(k)=-2Z_1i\sin(kr_0/2)$, respectively, with $z_1=-z_2=r_0/2$. (

(b) Transverse dicluster. Dicluster oriented in the ρ direction ($z_1=z_2=0$, $\rho_1=\rho_2=r_0/2$, $\varphi_1=0$, $\varphi_2=\pi$). Here one gets

$$\mathcal{F}_m^{(2-cl)}(k)=[Z_1+Z_2e^{-im\pi}]I_m(k\rho_0/2) \tag{47}$$

(for all m values). In particular, if $Z_1=\pm Z_2$ we get, $\mathcal{F}_m^{(2-cl)}(k)=2Z_1I_m(k\rho_0/2)$, where m takes only even values for $Z_1=Z_2$, and only odd values for $Z_1=-Z_2$.

(c) Angular average.

By performing the angular average of Eq. (45) with $\rho_1=\rho_2=r_0\sin(\theta)/2$, $z_1=-z_2=r_0\cos(\theta)/2$, $\varphi_2-\varphi_2=\pi$, one gets

$$\langle|\mathcal{F}_m^{(2-cl)}(k)|^2\rangle=(Z_1^2+Z_2^2)H_m(kr_0)+2Z_1Z_2e^{im\pi}G_m(kr_0) \tag{48}$$

in terms of the integrals,

$$H_m(x)=\frac{1}{2}\int_{-1}^{1}d\theta\sin(\theta)\left[I_m\left(\frac{x}{2}\sin\theta\right)\right]^2 \tag{49}$$

$$G_m(x)=\frac{1}{2}\int_{-1}^{1}d\theta\sin(\theta)\left[I_m\left(\frac{x}{2}\sin\theta\right)\right]^2\cos(x\cos\theta). \tag{50}$$

B. Dipoles

We consider now the case $Z_1=-Z_2$ in Eq. (45), and take the limit, $|Z_1|=|Z_2|\to\infty$, $r_0\to 0$, with $\mathbf{d}=Z_1\mathbf{r}_0=$ constant (*electric-dipole moment).*

This yields the *dipole form factor*

$$\mathcal{F}_m^{(dip)}(k)=\left[I_m'(k\rho_0)kd_\rho - iI_m(k\rho_0) \times\left(kd_z+\frac{m}{\rho_0}d_\varphi \right)\right] e^{-ikz_0}e^{-im\varphi_0}, \qquad (51)$$

where now ρ_0, z_0, φ_0 are the cylindrical coordinates of the dipole and d_ρ, d_z, d_φ are its components in the corresponding directions. This is the general result for dipoles within the channel.

In addition, we consider the case of random orientations of the dipole vector **d**. By performing the angular average over all possible orientations we get

$$\langle|\mathcal{F}_m^{(dip)}(k)|^2\rangle=\frac{1}{3}k^2d^2[I_m'(k\rho_0)]^2 + \frac{1}{3}k^2d^2[I_m(k\rho_0)]^2\left[1+\frac{m^2}{k^2\rho_0^2}\right]. \qquad (52)$$

Particular cases of interest for dipole motion along the axis of the channel ($\rho_0=0$) are now the following: (a) aligned dipole—parallel orientation (only $m=0$ term): $\mathcal{F}_0^{(dip)}(k)=kd$; (b) perpendicular orientation (only $m=1$ term): $\mathcal{F}_1^{(dip)}(k)=\frac{1}{2}kd$; and (c) angular average.

Here we obtain from Eq. (52), for $\rho_0\to 0$,

$$\langle|\mathcal{F}_m^{(dip)}(k)|^2\rangle=\frac{1}{3}k^2d^2\delta_{m,0}+\frac{1}{6}k^2d^2\delta_{m,1} \qquad (53)$$

Hence, in this case we get nonvanishing results only for $m=0$ or 1.

VII. CALCULATIONS

A. Swift ions in various materials

The application of the previous formulation to real materials requires first some analysis of the dielectric properties for each particular case. The materials of specific interest in relation with previous experiments include Ag and alumina. Figure 7 shows the energy-loss functions (ELF), Im $[-1/\varepsilon(\omega)]$, for these materials, according to the available data [25]. The solid lines are the experimental values while the dashed lines show approximate fittings to the data using simple models. These cases bear very different characteristics and so they will be analyzed separately.

1. Silver

The ELF of Ag [Fig. 7(a)] was fitted by a simple Drude model with parameters $\omega_{P0}=1.9$ and $\gamma=2.85$ a.u.; this yields an "effective" plasma frequency $\omega_{P-eff}=(\omega_{P0}^2-\gamma^2/4)^{1/2}=1.257$ a.u., or 34.2 eV. As it may be seen, this model yields only a rough representation of the average behavior of the ELF on a wide range of frequencies, including the dominant interband transitions around ω_{P-eff}, but the optical plasma resonance at 3.7 eV is outside this description.

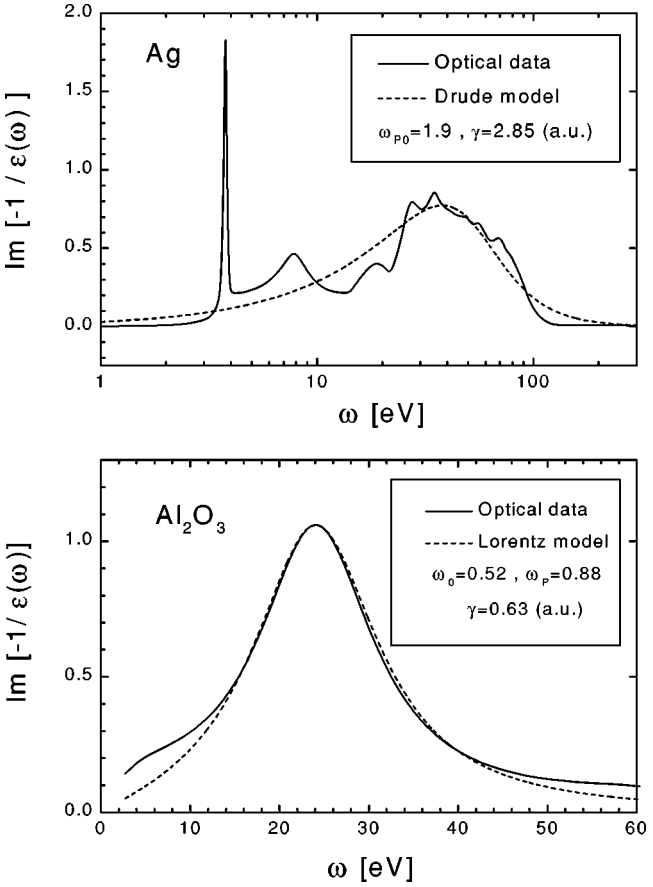

FIG. 7. Energy loss functions (ELF), Im$[-1/\varepsilon(\omega)]$, of Ag (a) and alumina (b). The solid lines are the experimental values [25] and the dashed lines show fittings to the data using simple models. In the case of Ag a Drude model has been used, with parameters $\omega_{P0}=1.9$ and $\gamma=2.85$ a.u.; corresponding to an effective plasma frequency $\omega_{P-eff}=(\omega_{P0}^2-\gamma^2/4)^{1/2}=1.257$ a.u. (34.2 eV). The low-energy plasma resonance at 3.7 eV is outside this rough fitting. The ELF of alumina was fitted by a Lorentz model with parameters $\omega_0=0.52$, $\omega_1=0.78$, and $\gamma=0.63$ a.u., corresponding to a plasma frequency $\omega_P=(\omega_0^2+\omega_1^2-\gamma^2/4)^{1/2}=0.883$ a.u. (24 eV).

Calculations were performed using both this simple model as well as the complete set of tabulated data, for the real and imaginary parts of $\varepsilon(\omega)$ [25], obtaining values of the induced potential and stopping force, from Eqs. (15) and (16), for protons moving within channels in Ag with radii $a=10$ and 20 Å . The protons are assumed to be moving along the channel axis, $\rho_0=0$ (the results for $\rho_0\neq 0$ would be larger than those obtained here). These calculations are shown in Fig. 8 (solid circles and dotted lines) as a function of the proton velocity. We observe from this figure that, in spite of its crudeness, the fitting model reproduces very well the results of the realistic description. These figures illustrate also the main characteristics of the problem; the shift in the values of the induced potential and stopping force are in accordance with the scaling predictions. In particular, it may be observed that the maximum stopping values drop by a factor 4 while the position of the maximum (indicated by vertical bars) shifts by a factor 2 for the present values of a.

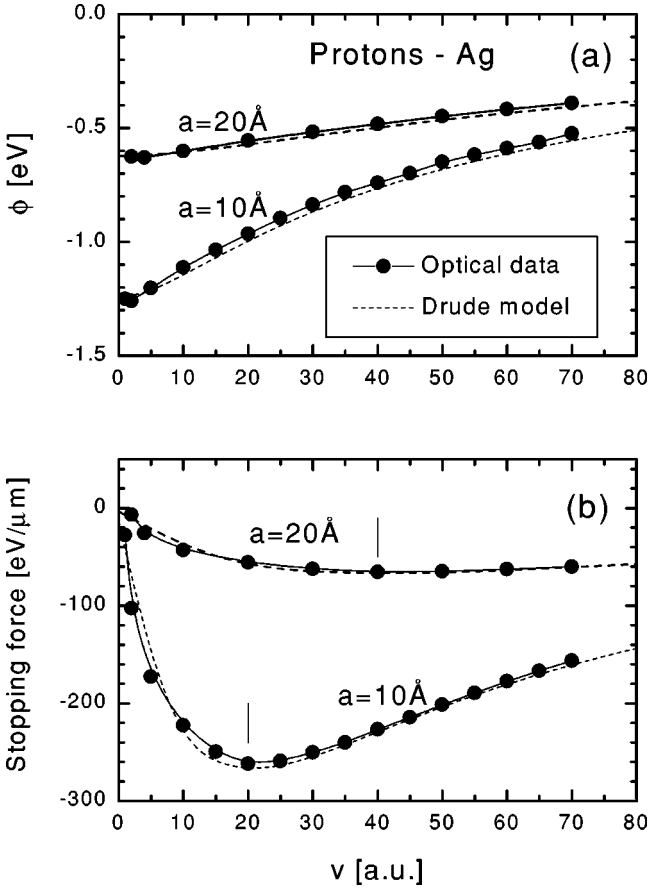

FIG. 8. Calculations of the induced potential (a) and stopping force (b), using Eqs. (15) and (16), for protons moving within channels in Ag with radii $a=10$ and 20 Å , as a function of proton velocity. The protons are assumed to be moving along the channel axis, $\rho_0=0$. The lines with solid circles are the results obtained by integration of the ELF data, while the dashed lines are the results obtained using the simple fitting model shown in Fig. 8.

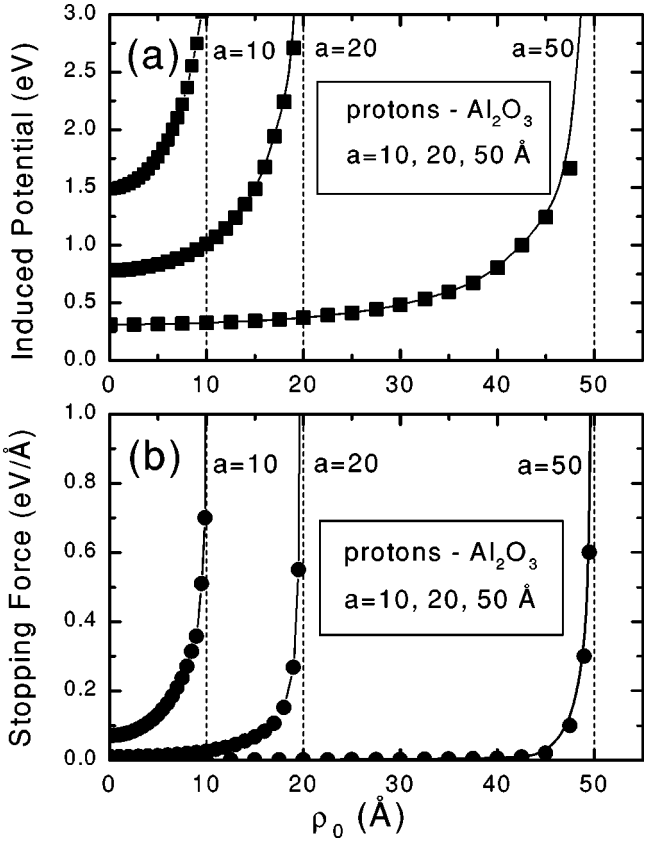

FIG. 9. Calculations of induced potentials and stopping forces for protons moving in alumina channels of different radii, $a=10$, 20, and 50 Å . Note the increasingly flat behavior throughout the inner region for large channel radius, and the importance of the interactions near the border, in a layer of thickness $\sim v/\omega_P$.

2. Alumina

A similar analysis of the dielectric properties was made for targets of Al_2O_3. The ELF of alumina is shown in Fig. 7(b), which includes the experimental data [25] and an approximate fitting using a Lorentz model with parameters $\omega_0=0.52$, $\omega_1=0.78$, and $\gamma=0.63$ a.u. The plasma frequency in this case, $\omega_P=(\omega_0^2+\omega_1^2-\gamma^2/4)^{1/2}$, takes the value 0.883 a.u., or 24 eV, which corresponds to the observable plasma frequency.

Calculations of induced potentials and stopping forces for protons moving in channels of different radii, $a=10$, 20, and 50 Å , are shown in Fig. 9. It is observed that as the radius increases not only the magnitudes of the induced potential and electric field decrease (as predicted by the scaling laws), but also that their behavior becomes flat, with the important values concentrated near the cavity walls, and within an interaction distance $\sim v/\omega_P$. The most critical effect is observed in the stopping force in panel (b).

A detailed analysis shows that the condition for the ''flat limit'' is that $x\equiv ka\gg 1$, and since the values of k of interest are $k\sim\omega_P/v$, this condition may be written as $a\gg a_{ad}$, being $a_{ad}=v/\omega_P$ the *adiabatic distance*. The stopping force in this limit takes the form of Eq. (31). In these conditions, the interaction with the walls is negligible through nearly all the internal region of the cavity, except only for a thin layer of thickness v/ω_P where the interaction is like that for plane surfaces.

Conversely, one can characterize the conditions to observe cylindrical curvature effects by $a\sim a_{ad}=v/\omega_P$. In this case the particle feels the effect of the surrounding walls. For the range of velocities of interest in ion-beam experiments one gets values of radii in the range $a\sim 5-50$ Å (i.e., in the nanoscale range).

B. Channeling of diclusters

We will illustrate here the application of the previous formulation to the case of diclusters channeled through narrow holes. One of the simplest cases is that of a pair of protons with correlated motion through the channel (this particular case bears some relationship with experiments with H_2^+ ions in solid foils, when the dissociation fragments are detected [26]).

Figure 10 shows the values of the energy loss of a pair of protons moving with various internuclear distances in a channel of radius $a=10$ Å in alumina. The center of mass

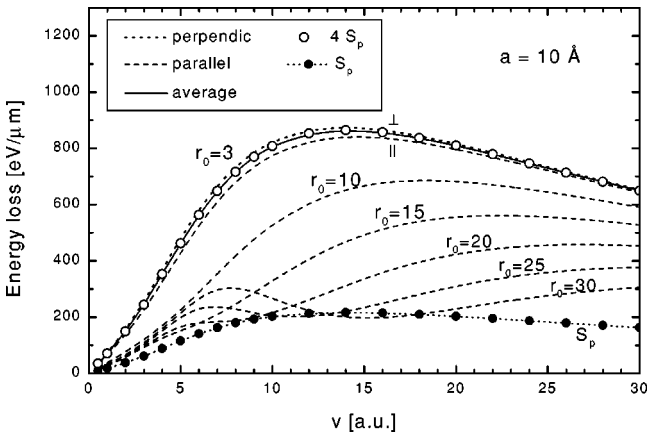

FIG. 10. Energy loss of a dicluster formed by a pair of protons moving with internuclear distances $r_0=3$, 10, 15, 20, 25, and 30 Å in a channel with radius $a=10$ Å in alumina. The dicluster moves along the channel axis. For $r_0=3$ Å the figure shows the cases of parallel (dashed), perpendicular (dotted line), and random (solid line) orientation of the internuclear axis. The set of curves for the other r_0 values corresponds to the case of parallel orientation. The solid circles show the proton-stopping values (S_p) for the same channel, whereas the open circles show four times these values ($4S_p$), which agrees closely with the angular average of the energy loss for $r_0=3$.

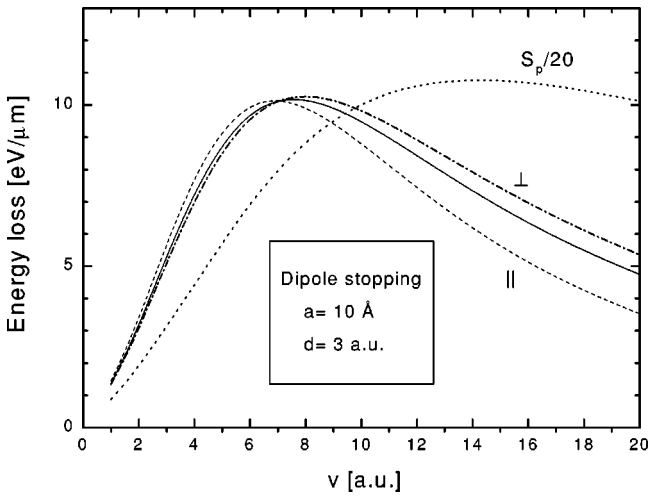

FIG. 11. Energy loss of a dipole moment $d=3$ a.u. moving along the axis ($\rho_0=0$) within a channel in alumina, with radius $a=10$ Å. The curves correspond to dipoles oriented parallel and perpendicular to the axis, and to the angular average of the energy loss. For comparison, the proton stopping divided by 20 ($S_p/20$), is also shown.

of the dicluster is on the channel axis. For the case $r_0=3$ Å we show the results for parallel, perpendicular, and random orientation (angular average). For the other radii (r_0 from 10 Å to 30 Å) we show only the case of parallel orientation. We also show for comparison the stopping values S_p for single protons channeled also along the axis (solid circles), and $4S_p$ (open circles) which is the limiting value for two united protons. The values of $4S_p$ nearly agree with the angular average of the diproton energy loss for the case $r_0=3$ Å. This indicates that the average energy loss in this case is nearly the same as if the two particles were united, even though the internuclear distance (3 Å) is not negligible compared with the channel radius. With increasing r_0 the differences in the stopping values become large, and important interference effects appear for r_0 values large that the channel diameter; these effects may be expected to arise in the case of dissociation of diatomic ions within narrow channels.

The case of nearly aligned diclusters may be of interest in relation to possible experiments with molecular ions. For instance, it would correspond to the Coulomb explosion (after break up) of H_2^+ ions, producing two correlated protons whose motion is confined to the channel walls. The present results are indicative of the magnitude of the expected ''vicinage effects,'' but a complete simulation would be required to compare with actual experiments.

C. Channeling of dipoles or polar molecules

The final question to be considered here is the interaction of electric dipoles with narrow channels. This question may be of interest for instance in experiments with excited neutral hydrogen atoms at the level $n=2$ (which has the property of spontaneous polarization, with a relatively large dipole moment, $d=3$ a.u.), or in experiments with polar molecules, like NaCl, LiF, HF, H_2O, or others (dipole moments: $d=3.3$, 2.6, 0.8, and 0.7 a.u., respectively). The conditions of very low electron densities within the channel may favor the possibility of transmission of unbroken molecules, which could not survive transmission in the usual experiments with solid foils.

It was observed in Fig. 10 that the energy loss of a pair of charges is not very sensitive to the internuclear distance if this is much smaller than the channel radius. Therefore, a first approach to the present problem can be made by considering the system as a simple electric dipole, according to the description given before, Eqs. (51)–(53). Figure 11 shows the calculated values of the energy loss of a dipole moment $d=3$ a.u. The results correspond to a dipole moving along the channel axis with radius $a=10$ Å. The curves correspond to dipoles oriented parallel and perpendicular to the channel axis, and to the angular average of the energy loss. We find here a larger orientational dependence than in Fig. 10, this is because of the angular dependence of the dipole field, in contrast to the dominant monopole interaction of Fig. 10. For comparison, the curve corresponding to the proton-stopping power divided by 20 is also shown. We conclude from this comparison that for such narrow channel the energy loss of a dipole may be 20 times smaller than that of a proton. In fact, the ratio of dipole to proton stopping depends strongly on the channel radius a. This ratio decreases rapidly with increasing radius (like $1/a^2$), since the dipole stopping decreases like $1/a^4$, whereas the proton stopping diminishes as $1/a^2$. This indicates the advantage of using narrow channels to test the energy loss of polar (atomic or molecular) systems. The magnitude of the energy loss indicates that the effect could be observable using nanochannels or nanotubes with several microns of length (note also that the present results correspond to the channel axis, so that they give lower bound estimations).

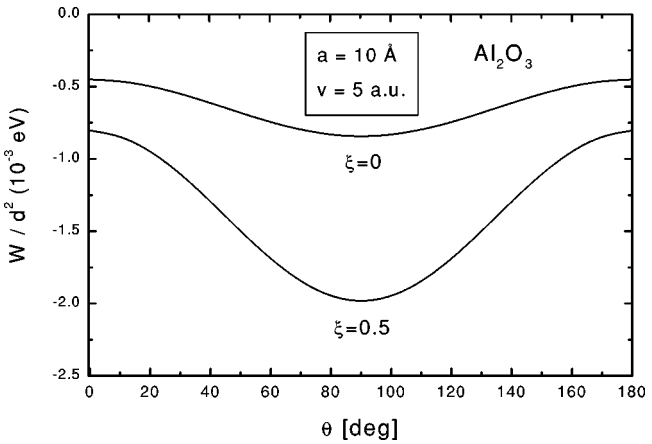

FIG. 12. Angular dependence of the self energy of a channeled dipole as a function of its angular orientation θ (the angle between the dipole moment $\vec{d}$ and the velocity $\vec{v}$), for $v=5$ a.u. and $a=10$ Å, and for two positions of the dipole within the channel, $\xi \equiv \rho_0/a=0$ and 0.5. The minimum energy value if obtained for $\theta=\pi/2$, corresponding to the transverse orientation of the dipole.

Finally, Fig. 12 shows the self-energy of a channeled dipole as a function of its angular orientation (the angle θ between the dipole moment $\vec{d}$ and the velocity $\vec{v}$). The minimum energy value if obtained for $\theta=\pi/2$, corresponding to the transverse orientation of the dipole. However, the magnitude of these values seems to be too small to have practical consequences.

VIII. SUMMARY

The significant advances in the production of channels and nanotubes in solids provides the possibility of new studies on the interaction of swift ions and molecules with these systems. Current studies of transmission of ions through microchannels are producing new information about the basic interaction processes and require also theoretical studies in the area.

In a previous formulation [16] several analytical results for a simple plasma-resonance dielectric function have been derived. Here the analysis was extended to incorporate more realistic descriptions of the dielectric properties of materials of experimental interest. The scaling properties of the induced field and forces have been derived, using a set of scaling functions to represent the general dependence in terms of reduced variables.

Based on this formulation, the magnitudes and the behavior of the expected energy losses and self-energies have been evaluated, for ions channeled in Ag and alumina targets. The influence of the dielectric properties on the calculated values has been shown and parametrized, and the size effects were characterized.

The formulation was extended to ion clusters or molecular composites, and the results were expressed in terms of a new type of form factors which incorporate the conditions imposed by the cylindrical geometry. The particular cases of the energy loss of dissociated or exploding diclusters, and the energy loss of channeled dipoles (with possible applications to the channeling of polar molecules or atoms) have been analyzed. Other possible applications may include the study of transient shifts of the atomic lines of moving ions, due to the effect of the induced potential, or the possible influence of the wake potential on the spectra of emitted electrons (field-acceleration effects).

The condition of low electronic density within the channel provides a unique environment that could be convenient for the design of novel experiments of transmission of single or correlated ions, neutral atoms and molecules. The general formulation and the results and ideas presented here could be useful for experimental studies and further advances along these lines.

ACKNOWLEDGMENT

This work was supported in part by ANPCYT of Argentina (PICT0303579).

[1] R. J. Warmack, R. S. Becker, V. E. Anderson, R. H. Ritchie, Y. T. Chu, J. Little, and T. L. Ferrell, Phys. Rev. B **29**, 4375 (1984).
[2] K. C. Mamola, R. J. Warmack, and T. L. Ferrell, Phys. Rev. B **35**, 2682 (1987).
[3] S. Iijima, Nature (London) **354**, 56 (1991); **356**, 776 (1992).
[4] T. W. Ebbesen and P. M. Ajayan, Nature (London) **358**, 220 (1992).
[5] A. Thess *et al.*, Science **273**, 483 (1996).
[6] V. P. Dravid *et al.*, Science **259**, 1601 (1993).
[7] P. M. Ajayan, S. Iijima, and T. Ichihashi, Phys. Rev. B **47**, 6859 (1993).
[8] L. A. Bursill, P. A. Stadelmann, J. L. Peng, and S. Prawer, Phys. Rev. B **49**, 2882 (1994).
[9] G. V. Dedkov, Nucl. Instrum. Methods Phys. Res. B **143**, 594 (2000).
[10] L. A. Gevorgyan, K. A. Ispiryan, and R. K. Ispiryan, Pis'ma Zh. Eksp. Teor. Fiz. **66**, 304 (1997) [JETP Lett. **66**, 322 (1997)]; Nucl. Instrum. Methods Phys. Res. B **145**, 155 (1998).
[11] Y. Yamazaki, S. Ninomiya, F. Koike, H. Masuda, T. Azuma, K. Komaki, K. Kuroki, and M. Sekiguchi, J. Phys. Soc. Jpn. **65**, 1199 (1996); Phys. Rev. Lett. **78**, 4557 (1997).
[12] K. Tökési, L. Wirtz, and J. Burgdörfer, Nucl. Instrum. Methods Phys. Res. B **154**, 307 (1999); K. Tökési, L. Wirtz, C. Lemell, and J. Burgdörfer, *ibid.* **164-154**, 504 (2000).
[13] Y. T. Chu, R. J. Warmack, R. H. Ritchie, J. Little, R. S. Becker, and T. L. Ferrell, Part. Accel. **16**, 13 (1984).
[14] M. Schmeits, Solid State Commun. **67**, 169 (1988).
[15] N. Zabala, A. Rivacoba, and P. M. Echenique, Surf. Sci. **209**, 465 (1989).
[16] N. R. Arista and M. A. Fuentes, Phys. Rev. B **63,** 165401 (2001).

[17] N. R. Arista, Nucl. Instrum. Methods Phys. Res. B **164-165**, 108 (2000).
[18] C. A. Walsh, Philos. Mag. B **63**, 1063 (1991).
[19] J. D. Jackson, *Classical Electrodynamics* (Wiley, New York, 1975).
[20] R. H. Ritchie, Phys. Rev. **106**, 874 (1957).
[21] I. Abril, R. García-Molina, C. Denton, J. Pérez, and N. R. Arista, Phys. Rev. A **58**, 357 (1998).
[22] P. M. Echenique, R. H. Ritchie, and W. Brandt, Phys. Rev. B **20**, 2567 (1979).
[23] P. M. Echenique and A. Howie, Ultramicroscopy **16**, 269 (1985); N. R. Arista, Phys. Rev. A **49**, 1885 (1994).
[24] T. L. Ferrell, P. M. Echenique, and R. H. Ritchie, Solid State Commun. **32**, 419 (1979).
[25] H. J. Hagemann, W. Gudat, and C. Kunz, J. Opt. Soc. Am. **65**, 742 (1975); DESY Report No. SR-74/7, 1974 (unpublished).
[26] D. S. Gemmell, Nucl. Instrum. Methods **170**, 41 (1980); Nucl. Instrum. Methods Phys. Res. **194**, 255 (1982).